Atomic resolution analytical microscopy

by P. E. Batson

It is possible under favorable circumstances to identify composition, bonding, and electronic structure with atomic resolution in microelectronic device structures. In current device structures, where only a few interface atoms can dominate the performance of a device, this can contribute important understanding relevant to product development. This paper is a brief overview of work in our laboratory using scanning transmission electron microscopy to achieve such capabilities.

Introduction

Many modern device structures are critically dependent on the properties of a very small number of atoms which reside at heterogeneous interfaces. For instance, the mobility of electrons in a field-effect transistor depends on the density of defect states at the Si/SiO_2 interface next to the conduction channel. Intermixing of nitrogen within SiO_2 can produce better dielectric material for DRAM capacitor isolation. Small, deliberately induced strain in a thin Si layer produces a high-mobility channel for very fast transistors, but misfit dislocations at the substrate interface of the channel can limit the practical use of such a layer [1, 2]. Layers of material only 2–3 atoms thick can produce a hundredfold change in the contact resistance of a silicon/polysilicon (Si/poly-Si) structure.

The transmission electron microscope (TEM) has been used for many years to investigate the morphology and atomic structure of microelectronic device structures, while their analytical properties—electronic structure and chemical composition and bonding—have been the subject of surface-sensitive, medium-resolution techniques: ellipsometry for oxide thickness and dielectric determinations, deep-level transient spectroscopy and capacitance–voltage measurements for defect electronic structure, X-ray diffraction for crystal strain, and secondary ion mass spectroscopy (SIMS) for composition. A device structure imaged using a TEM could be identified by inference with such analytical properties.

Today we face the problem that devices are too small for reliable, routine diagnosis using surface-sensitive, low-resolution probes. For instance, it is very difficult to investigate the composition of a DRAM capacitor trench sidewall by means of SIMS. The uncertainties in probed area, secondary ion yield for non-normal probe incidence, and the buried nature of the interface all limit the lateral resolution to about 50 nm and the depth resolution to about 5 nm [3]. The many new techniques derived from the scanning tunneling microscope (STM) satisfy some of those needs, particularly for dimensional metrology, but suffer from their surface-oriented nature when confronted with a morphologically complicated shape [4].

In this paper, we present a brief overview of the use in our laboratory of the scanning transmission electron microscope (STEM) to fulfill some of those needs. It is fundamentally analytical in nature in that it is designed

0018-8646/00/$5.00 © 2000 IBM

not only to determine atomic structure, but also to obtain information on the composition and atomic bonding environment of a specimen. Scanning transmission electron microscopy, like SIMS and scanning electron microscopy, is based on the use of an electron probe. It shares with the TEM a high-resolution capability to locate atom positions; it shares with SIMS an ability to distinguish the kind of atoms that are present and how they are bonded; and it shares with the scanning electron microscope (SEM) a simplicity of interpretation grounded in its scanning nature. As we see below, under some circumstances it can also provide atomic-resolution electronic structure information similar to that obtained from large areas by optical absorption. It is also fundamentally a bulk-sensitive probe—it can, for example, be used to obtain information within a localized but subsurface region that controls the operation of a microelectronic device.

Annular dark-field imaging in the STEM

The STEM is a medium-energy (100–300 keV) instrument that works with standard TEM specimens. Therefore, it utilizes the expertise and infrastructure that have been developed over the years to integrate the TEM into the device development process [5]. The instrument in our laboratory is a modified VG Microscopes HB501 STEM which produces a 0.2-nm-diameter electron probe at an electron beam energy of 120 keV. Illustratively, **Figure 1** shows a low-magnification STEM image of a DRAM FET-trench capacitor structure. The annular dark-field (ADF) image shown was obtained using large-angle elastic scattering, which is sensitive to the atomic number of the material [6–8].

Figure 2 depicts the ADF imaging method. Shown there is a schematic illustration of the electron-scattering geometry in the STEM. Electrons are scanned in a raster across the specimen; they travel through the specimen and are caught by various detectors which feed video displays for viewing. The STEM is therefore a combination of a high-resolution TEM instrument with a low-resolution SEM. In ADF imaging, we rely on the fact that an electron which passes near an atom in a specimen will suffer a large electrostatic deflection. If we place a detector well away from the undeflected beam direction, we can obtain a signal using only the electrons that have been deflected through large angles and which have therefore passed close to an atom column. If the probe is smaller than the distance between the atom columns, about 0.3 nm for the [0 1 1] orientation of Si, this detection method yields a large change between the on-column and off-column positions of the probe. The detected intensity is roughly proportional to the number of atoms in the column times the square of their atomic number [9]. Thus, we have a signal that gives us information about the locations of the atoms, their concentration, and their atomic numbers.

This imaging technique was pioneered in the 1970s by Crewe, who was the first to show atomic resolution and single-atom sensitivity with atomic number contrast using a scanned electron probe [6]. More recently, the technique has received extensive investigation for imaging interface and defect structures in crystals [7, 8]. Because the technique is sensitive to the atomic number (Z) of the atom, ADF imaging is sometimes referred to as "Z-contrast." Therefore, brighter areas are those composed of more atoms or atoms having a higher atomic number. In Figure 1, the Si matrix and Si_3N_4 dielectric are more dense and therefore brighter than the SiO_2 dielectric. Because an ADF STEM signal averages over many scattering angles, there is less contrast arising from diffraction than is normally observed in a TEM. In the figure, the Si matrix surface is above; the poly-Si-filled trench capacitor extends several microns below into the substrate, and is bounded by an $SiO_2/Si_3N_4/SiO_2$ dielectric insulating layer along the trench sidewalls. There is a poly-Si strap connecting the top of the capacitor with the Si matrix region that would become the drain end of a FET in a completed device. The contrast in this image is primarily due to material density, with the most dense areas causing the most scattering into the high-angle detector.

Figure 3 is a composite of higher-magnification ADF images of the trench dielectric. Intensities are roughly proportional to atomic density, so that the Si matrix and poly-Si capacitor appear with the same brightness. Variations reflect grain boundaries and orientation differences in the poly-Si. SiO_2 appears darker than Si. Within the 15-nm dielectric, we can image three regions—associated with the presence of SiO_2, Si_3N_4, and SiO_2. Bright-field (BF) imaging in this area would show no variation in contrast within the dielectric. There appears to be a 2–3-nm-thick region of brighter contrast following the edge of the Si matrix. Identification of this requires higher magnification and atomic-resolution analytical information, to be discussed next.

Atomic column imaging

The diagram in Figure 2 suggests that if our probe is small enough and the crystal is oriented with the atom columns lined up with the electron beam direction, we should see bright spots corresponding to the atom column positions. In **Figure 4**, a $Ge_{30}Si_{70}/Si$ interface is shown using (a) small-angle BF imaging, equivalent to a standard TEM result, and (b) ADF imaging. The BF image consists of many overlapping fringes that convey the projected symmetry of the lattice. However, since their precise position is strongly dependent on focus conditions, they cannot be interpreted as positions of atoms. In addition,

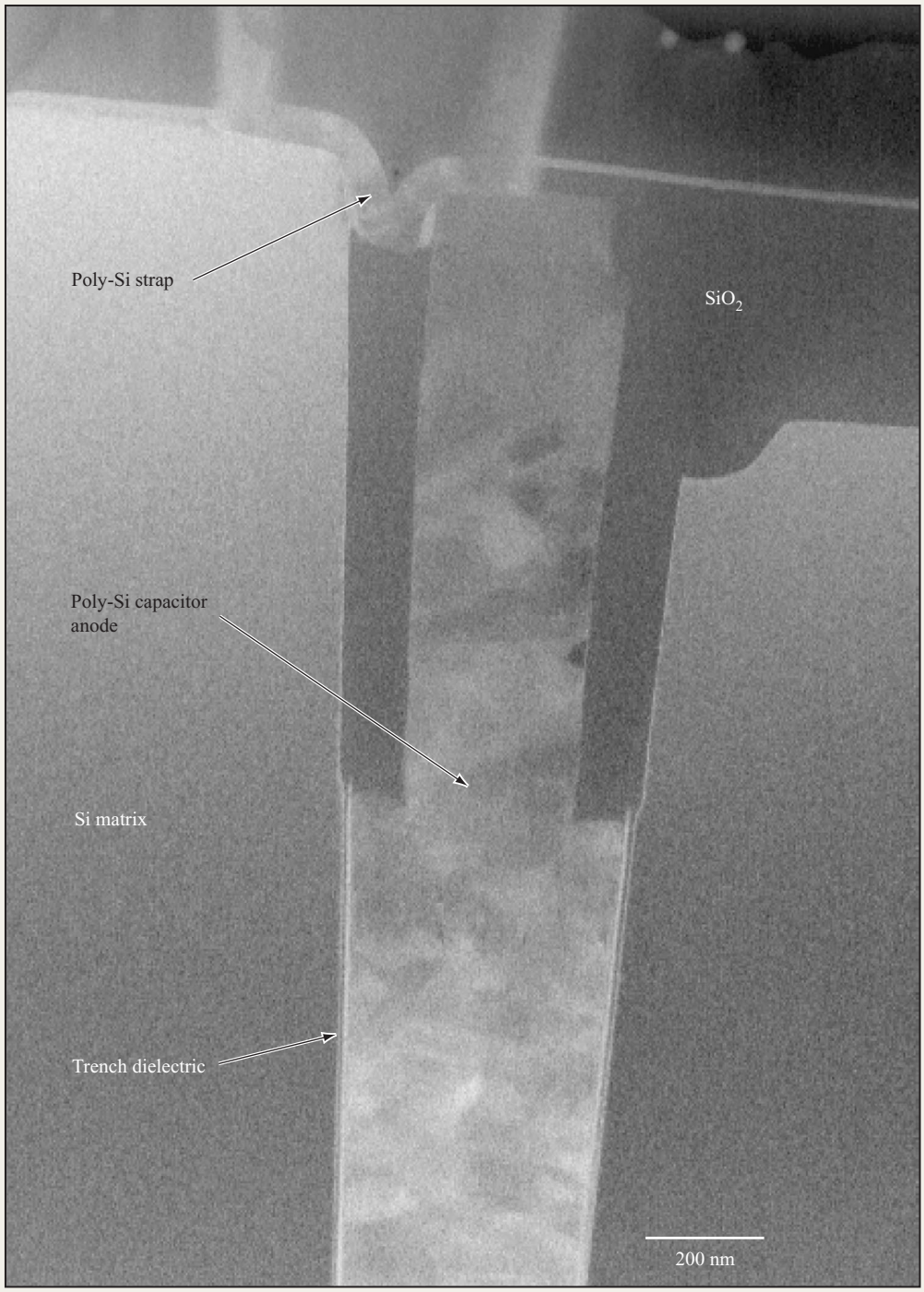

Figure 1

Low-magnification ADF image of an FET-trench capacitor structure under development for use in a DRAM chip. A poly-Si strap connects the Si matrix to the storage capacitor at the upper portion of the image; the capacitor extends several μm into the Si matrix; and the trench dielectric isolates the poly-Si capacitor element from the Si matrix.

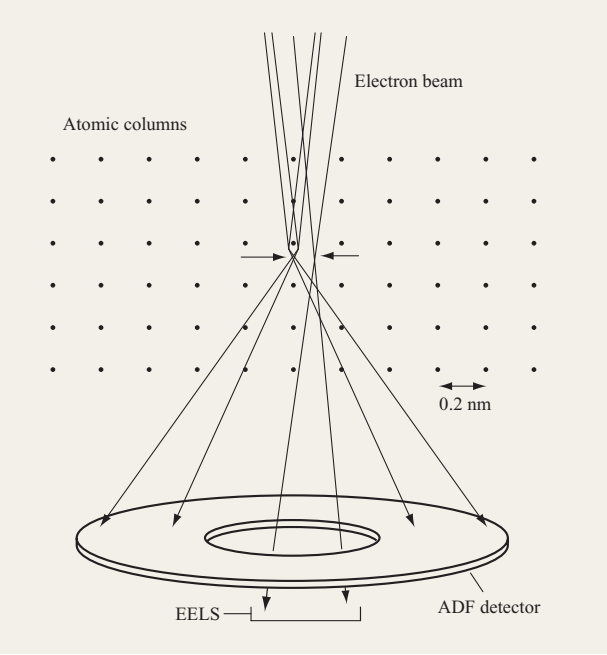

Figure 2

Scattering geometry for ADF imaging and spatially resolved EELS analysis. The STEM forms a 0.2-nm-diameter probe of electrons which travel through a thin section of the specimen. If the probe travels near a column of atoms, it is elastically deflected to large scattering angles, where it is intercepted by an annulus-shaped detector. An aperture located on the optic axis admits electrons undergoing small-angle scattering into an electron energy loss spectrometer for EELS analysis. As the probe is scanned in a raster over the specimen, the ADF detector generates a video signal for display.

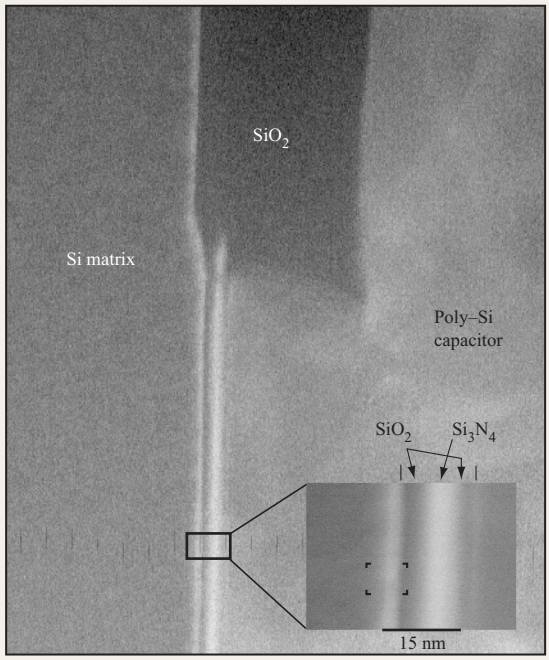

Figure 3

Trench dielectric region of the capacitor of Figure 1. The ADF imaging produces a strongly atomic-density-sensitive image, so that areas consisting of SiO_2 are clearly distinguished from areas of Si_3N_4. A bright region appears to lie within the Si matrix sidewall. The small corner brackets in the inset define this region for Figure 5.

they carry very little information about the atomic number. Therefore, the position of the composition interface is not visible in this image. In the ADF image, bright spots correspond directly to atomic columns, with their brightness indicating the average atomic number for equal column lengths, so the composition interface is clearly visible. The image is almost independent of focus and thickness, making ADF imaging a very useful and practical technique for imaging heterogeneous crystals.

In this image, each spot corresponds to a double column, with the column separated by 0.14 nm in the [1 1 0] projection. Since the STEM probe diameter in this experiment was 0.2 nm, the columns are not resolved, appearing instead to be single spots elongated in the [1 0 0] direction (left–right) in the image. Returning to the DRAM structure, **Figure 5** shows a further magnification of the small bracketed area in the inset of Figure 3. This image clearly shows elongated spots ending at the Si/SiO_2 interface at the trench sidewalls. We can now see that the narrow region of bright contrast in the lower-magnification images does indeed coincide with the Si lattice. The crystal structure appears relatively unmodified except for the ADF intensity variation. Further understanding of this result requires an analytical analysis of bonding or composition, as discussed below. At this point, however, it can certainly be inferred that atomic-resolution images of technologically interesting structures are readily obtainable by means of an STEM, with the apparent limit being imposed by instrumental probe size limitations rather than specimen preparation.

Analytical analysis using electron energy loss spectroscopy

Returning to Figure 2, we note that that figure also depicts an alternative analytical signal using electrons that do not suffer a large deflection. These sample primarily the areas between atoms, and scatter mainly by loss of energy to valence and conduction electrons within the specimen. They are therefore sensitive to its composition,

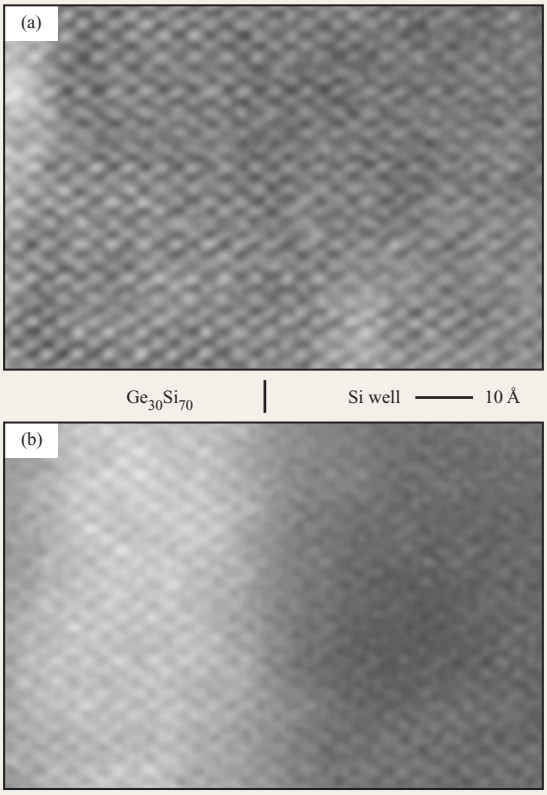

Figure 4

(a) Bright-field image of a Si/$Ge_{30}Si_{70}$ interface. The bright spots give correct atomic periodicities but are not located correctly relative to corresponding atom positions. There is little atomic number sensitivity. (b) The ADF image gives spots elongated in the (0 0 1) direction, corresponding to the "dumbbell"-shaped double atom columns. There is a good registry of the image with the atomic lattice, and the brightness of the spots bears a close relationship to the atomic numbers of the atoms in each column. Adapted from [30], with permission.

bonding, and electronic structure. With an electron spectrometer placed on the optic axis of the STEM, we can use electron energy loss spectroscopy (EELS) to obtain information about the energy lost by electrons in the probe as they traverse the specimen [10]. The most important loss features for this work are absorption edges caused by electronic transitions from atomic core levels to the conduction band (CB). These identify the particular type of atom from their onset energy and summarize the symmetry-projected CB local density of states (LDOS) and local bonding configuration by their shape.

Figure 6 shows an illustrative EELS spectrum for Si in the 0–120-eV energy loss range. For a sample 50–100 nm thick, most of the incident electrons do not lose any

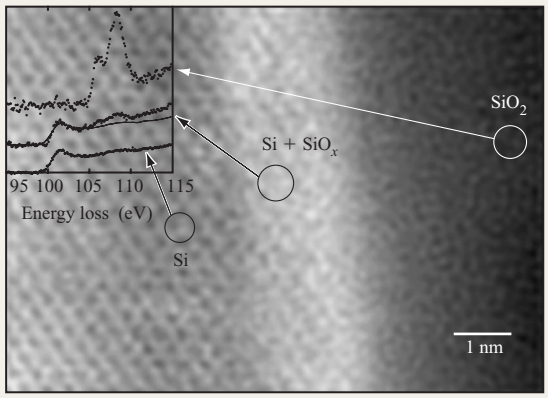

Figure 5

High-magnification ADF view of the bright region in the trench sidewall of Figure 3. This view shows that the region clearly lies within the crystalline region. EELS spectra in the inset suggest that the interface is rough on a scale of 1 nm, with SiO_2 and crystalline Si in intimate contact, or that O has been driven into the Si matrix during the cleaning and growth of SiO_2 on the trench sidewalls.

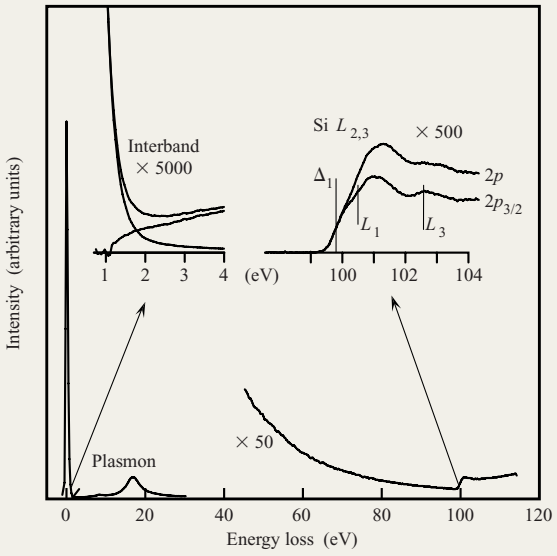

Figure 6

Illustrative EELS spectrum for silicon. Effects can be seen due to no-loss electrons at 0 eV, plasmon losses at 17 eV, the Si 2*p* core to CB absorption edge at 100 eV, and direct interband absorption near 1 eV. The fine structure on the core edge can be examined for structure in the CB LDOS. Direct interband information is difficult to obtain because the scattering cross section is only about 1% of the background intensity near 1 eV.

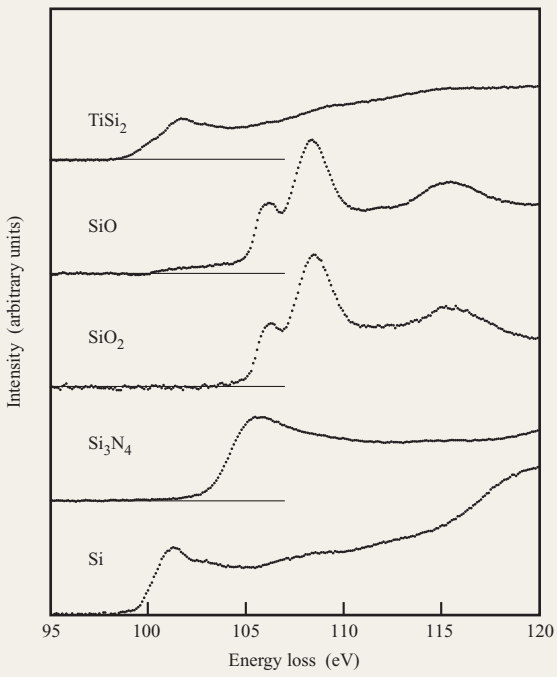

Figure 7

EELS spectra due to Si $2p$ core absorption edges, for several compounds. These show variation of structure on the 5-eV scale and can be used for "fingerprint" identification of unknown regions of a specimen.

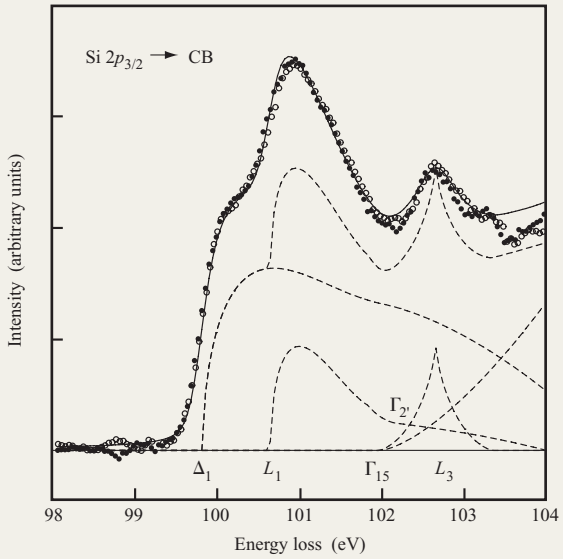

Figure 8

Details of the Si $2p_{3/2} \rightarrow$ CB absorption edge obtained via EELS after background subtraction. The Brillouin zone critical points Δ_1, L_1, and L_3 are clearly resolved. In addition, the edge shape may be modeled to obtain likely positions of $\Gamma_{1,5}$ and $\Gamma_{2'}$. Two sets of experimental data are shown to illustrate the excellent reproducibility achievable using EELS. The edge position can be obtained with an accuracy of ± 20 meV.

energy and therefore end up in the no-loss peak centered at 0 eV energy loss. The second large peak near 17 eV results from electrons that lose energy to one collective electronic excitation, or plasmon. This excitation involves all of the valence electrons in the solid and so is characteristic of electron density, but is less informative about the bonding or electronic structure. Near 100 eV for Si, an absorption edge is evident for electronic transitions from the $2p$ core levels to the CB. This feature is only about 1% as strong as the plasmon peak. As summarized in the magnified insert, there is fine structure within 2 to 3 eV of the core loss onset energy, giving information about the CB in the solid. Finally, in the 1–3-eV region, near the no-loss peak, there is a direct interband absorption edge present which is caused by energy loss via direct excitation of single electrons across the bandgap. This is only about 0.01% as large as the no-loss peak and is therefore very difficult to observe [11]. High-energy-resolution optical spectroscopy has been obtained in this energy range by cathodoluminescence (CL) using micron-sized electron beams [12], and energy-integrated CL has been obtained in the STEM using small beams [13]. However, EELS is the only STEM-based signal that promises to obtain both energy and spatial resolution to allow investigation of a semiconductor bandgap, and so it is currently the subject of experimental and instrumental investigation [14, 15].

Therefore, core-to-CB absorption has enjoyed the most widespread use as an analytical signal because it has been relatively easy to obtain and is usually quite specific to composition. In **Figure 7** several Si $2p_{3/2} \rightarrow$ CB spectra are shown for different Si bonding environments. These shapes can be used to identify the Si compounds with the lateral spatial resolution limited by the probe size even when analyzing single atom columns [16]. We can use this to understand the trench sidewall image in Figure 5, where EELS from three areas are displayed in the figure insert. They show clear signatures for the bulk Si and SiO_2 in regions a few atomic layers away from the interface. Within the narrow transition region, a composite shape is observed, one consisting partly of Si and partly of SiO_2, in spite of the fact that a clear Si atomic lattice is present. It seems likely, therefore, that this interface is not smooth in the [1 1 0] imaging projection. This might happen if oxygen is driven into the interface during cleaning, or possibly if the cross-sectioned region did not precisely cut

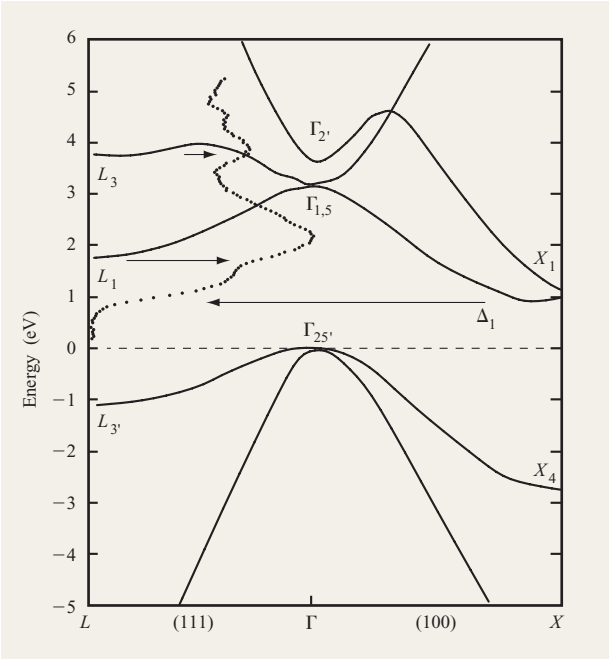

Figure 9

Interpretation of the Si $2p_{3/2} \rightarrow$ CB absorption. An experimental result is plotted over the Si band structure. Regions of the Brillouin zone that are dipole-allowed and that have a large effective mass contribute to the spectrum. Final states at L_1, Δ_1, and L_3 are allowed. Scattering to final states at the Brillouin zone center at Γ is forbidden.

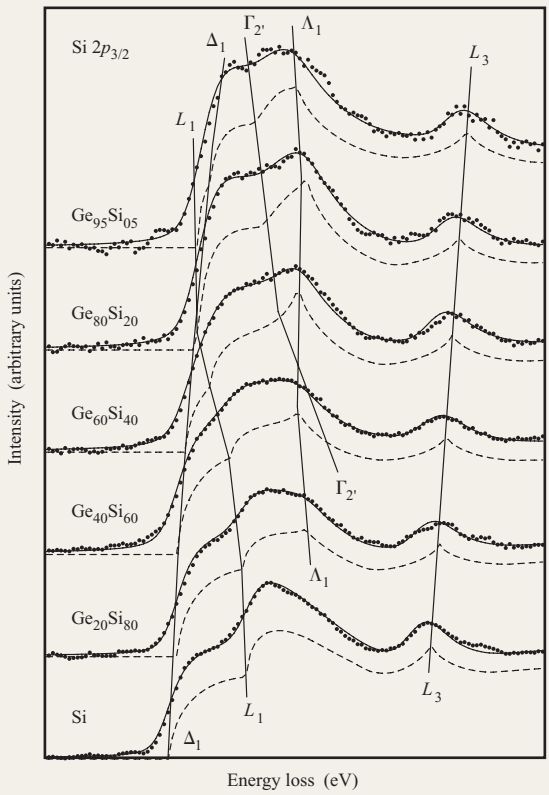

Figure 10

Summary of evolution of Si $2p_{3/2} \rightarrow$ CB absorption edges as a function of alloy composition in $Ge_{1-x}Si_x$. Brillouin zone critical points are made obvious by their systematic shifts with alloy composition. Brillouin zone center movement can be inferred in spite of the dipole selection rules. Λ_1 denotes a saddle point which is absent in Si but appears in Ge as the critical point $\Gamma_{2'}$ descends and becomes a local band minimum. Adapted from [30], with permission.

the curved trench sidewall perpendicular to its surface. This kind of imaging and spectroscopic behavior has also been observed by others at the Si/SiO_2 interface in thin gate dielectrics, where interface roughness has been cited as a possible cause [17].

At a somewhat more detailed scale, the elemental Si absorption edge itself can be interpreted for CB information. In **Figure 8** two Si $2p_{3/2}$ absorption edges are shown. These edges have been extensively processed by 1) subtraction of a slowly varying background, 2) deconvolution of an experimental instrumental resolution function, and 3) removal of structure derived from the spin-orbit splitting of the spin 3/2–1/2 core states. The data are then compared with model spectra derived from trial *s*,*d*-symmetry-projected LDOS curves. These curves are generated analytically, assuming that each symmetry-allowed band edge may be expanded in a parabolic fashion about the band minimum. The band minimum and carrier effective mass are then considered to be fitting parameters for comparison with the measured data.

Figure 9 shows a typical band structure for Si [18]. There are three main symmetry-allowed CB final states: 1) the *s*-like minimum at Δ_1, dispersing in the [1 0 0] direction; 2) the *s*-like minimum in the [1 1 1] direction L_1; and 3) the *d*-like saddle point at L_3 in the [1 1 1] direction. Data for the Si core absorption are plotted over the diagram to show how the features of the spectra correspond to features of the bands. We can create a trial LDOS for the comparison to the data by summing LDOS along the allowed bands. If a band is particularly flat in energy, an inflection point is generated in the LDOS. Finally, experimental effects are included, such as distortion by the core exciton, core lifetime broadening, and instrumental resolution to produce the solid curve fit to the experimental data in Figure 8. This spectral processing is discussed in detail in [19].

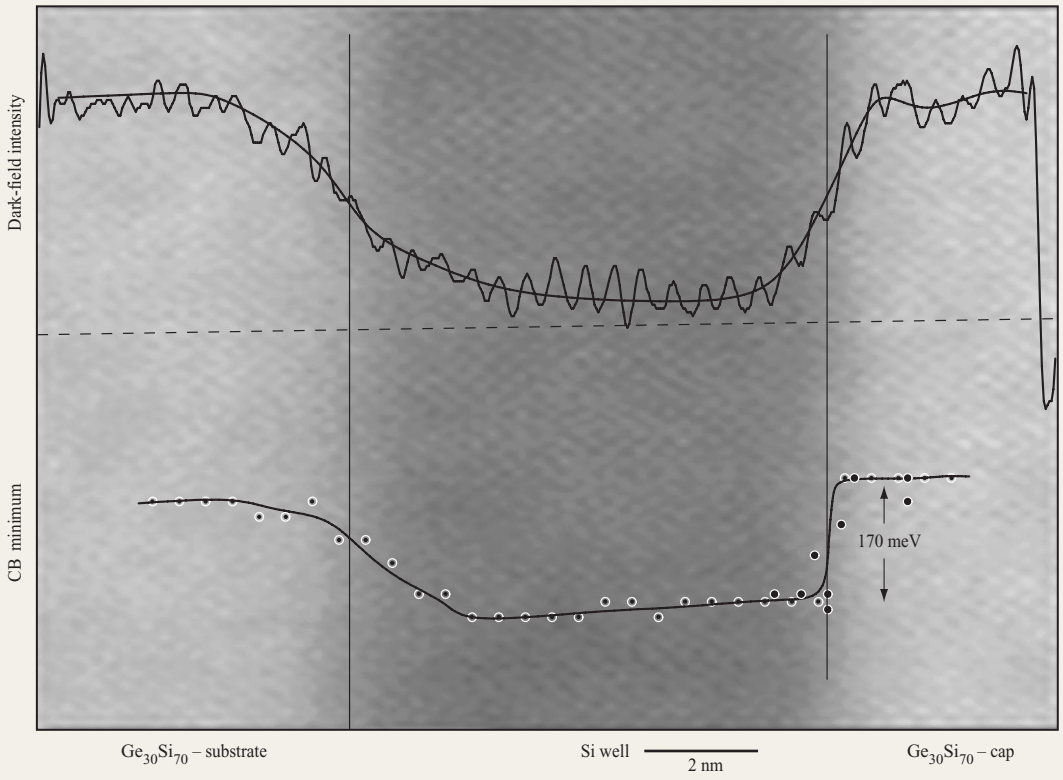

Figure 11

Strained Si quantum well confined between a $Ge_{30}Si_{70}$ substrate (left) and cap (right). The substrate composition was graded to reduce the impact of misfit strain. The upper curve is an ADF line scan along the dashed line. The lower curve is an EELS measurement of the CB minimum along a similar line. The heterojunction band offset can be accurately measured. Adapted from [30], with permission.

As is clear from Figure 8, this procedure gives excellent reproducibility. The two sets of experimental results in that figure were from the Si substrate and Si capping layer in a $Ge_{30}Si_{70}$ quantum well structure [20]. The positions of Δ_1, L_1, and L_3 are clearly reproduced, with better than 20-meV accuracies. In the relaxed $Ge_{30}Si_{70}$ alloy, these major CB points have shifted systematically. We have followed the evolution of these values throughout the relaxed Ge_xSi_{1-x} alloy series and find, as shown in **Figure 10**, that the CB follows very closely the predicted behavior as a function of Ge content [21]. In fact, we find on completion of this exercise that the Si 2*p* core level is constant in energy in the relaxed alloy, allowing the use of the absorption edge position to track the band offset in this system [22].

With some minor assumptions regarding strain, we can even use these results to obtain the band offset in a strained quantum well [23]. This is illustrated by **Figure 11**, in which we have obtained the heterojunction CB offset as a function of position across a 9-nm strained Si well. In the figure, we show an ADF image of the well which shows the atom columns and identifies the position of the well by atomic number (*Z*-contrast). A line scan of the recorded intensity along the dotted line is shown in overlay. The position of the CB is obtained from EELS spectra and is also recorded on the image. This structure contains a deliberately introduced grading of the composition on the substrate side of the well, readily visible in the ADF line scan on the left. The band offset obtained clearly follows this composition variation on the left as well. At the upper interface (to the right), where quantum well conduction is desired, the composition is made as discontinuous as possible. A surprising result is that the EELS CB offset variation is sharper than the composition profile at the upper interface. This could be the result of "over-strain" at the interface, a condition

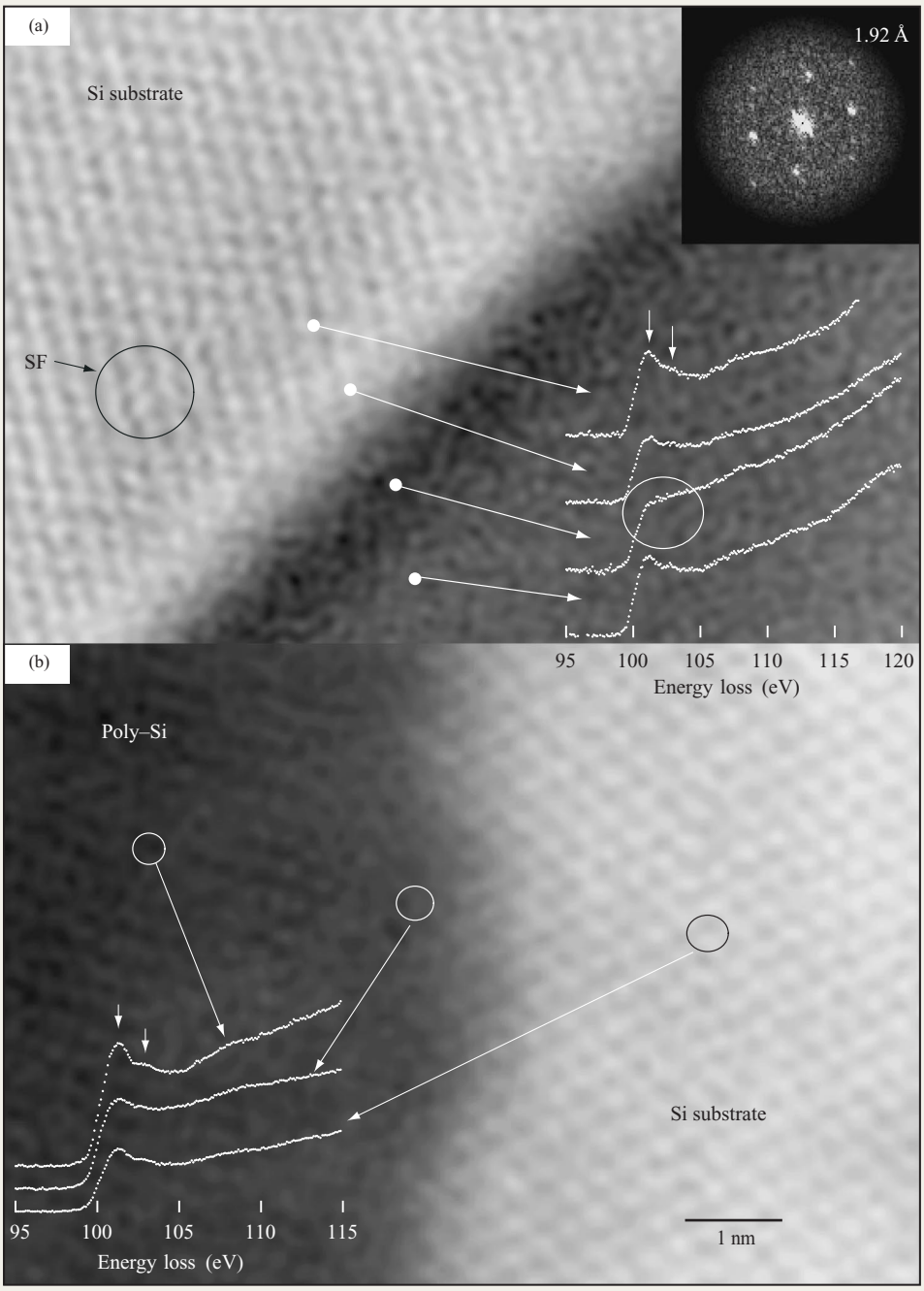

Figure 12

(a) ADF image and EELS spectra for a high-resistance Si/poly-Si interface. Si $L_{2,3}$ spectra show a modification of the near-edge structure that indicates the presence of a region of poor conductivity within 1 nm of the interface. (b) ADF image and EELS spectra for a low-resistance Si/poly-Si interface. The $L_{2,3}$ edges remain peaked, with no evidence for a heterogeneous layer at the interface. From [15], with permission.

that has been suggested previously to be present in Si–Ge multilayers, but which has not been conclusively identified [24, 25].

How might this very fine structure be exploited in the case of the DRAM structure of Figure 1? This particular structure was fabricated to test the electrical integrity of the strap connection between the drain of a DRAM access transistor and a poly-Si region of a DRAM capacitor. It was found that under some circumstances, the resistance of the strap connection appeared to be 100 times bigger than normal. However, TEM inspection of the structure showed no obvious reason for the behavior. In **Figure 12(a)**, the Si/strap interface from the upper portion of Figure 1 is shown at high magnification in ADF imaging. The Si substrate is on the left; the poly-Si strap is on the right. Si 2*p* absorption spectra are shown at the lower right. It is clear from the image that there is a 1-nm-thick region of low density at the interface. The $2p \rightarrow$ CB absorption results show that this region is largely composed of Si, although a minor amount of O may be present. The Si edge shape is distinctly bulklike on either side of the interface, but within the interface is less sharp, with the loss of fine structure attributable to the bulk bands. This behavior has been observed in fine Si particles and in other Si objects in confined situations [26, 27]. It appears therefore that the poly-Si growth interface, although primarily Si in composition, is disordered on a 1-nm scale, leading to a lower density and to damping of the CB structure by electron confinement effects. Inspection of the ADF image 1–2 nm deep into the Si substrate provides a possible explanation for this behavior. Si stacking fault (SF) structures are visible (circled), suggesting that the reactive ion etch (RIE) cleaning, used to prepare the Si surface for growth of the poly-Si strap, caused subsurface damage that led to the development of surface stress that inhibited growth.

Figure 12(b) shows an example of an analysis of a low-resistance strap interface. This interface has an almost uniform density with no discernible interface layer. In fact, the interface is rough at the 0.5-nm level, indicating intimate contact between the Si substrate and the poly-Si strap. The EELS spectra show bulklike fine structure throughout. No subsurface defects are visible. It is intriguing to note that the interface does show some blurring of the CB fine structure, suggesting that the interfacial quality is not yet as good as it could be, and that some improvement in electrical characteristics may therefore be possible with further work on this interface.

Conclusions and future directions

This analytical technique clearly provides a way to deduce the atomic arrangement and local bonding in heterogeneous devices. Further, it can provide clues about specific effects that the local atomic arrangement has on the macroscopic operation of such devices, facilitating device design. Clearly, however, these results show some weaknesses. The 0.2-nm probe size limits the available information about local structure, and the 0.2-eV energy resolution precludes the routine use of EELS to obtain a local bandgap. Both of these weaknesses are being addressed, the first with improved electron optics that will produce a 0.1-nm or better electron probe at 120 keV [28], and the second with addition of an electron monochromator in the electron source region [29]. With the addition of these capabilities, it should be possible to obtain the atomic arrangement at crystalline/amorphous interfaces. It should also be possible to obtain both the CB information and the position of the valence band (VB) edge from the bandgap information. Finally, it may also be possible to obtain direct information about near-edge and deep electronic gap states associated with crystal point defects. It appears that electron microscopy, far from being a mature field after more than 60 years of development aimed at imaging crystalline structure, is poised at the threshold of new capability that will allow it, ultimately, to identify the position, identity, bonding, and electronic behavior of individual atoms in complicated microelectronic structures.

Acknowledgments

The author wishes to thank P. Flaitz and A. Domenicucci for collaboration in analysis of the DRAM structure. The work with GeSi alloy structures benefited from collaboration with J. F. Morar, F. K. LeGoues, K. Ismail, and P. Mooney. The author also acknowledges extensive discussion with J. Silcox, D. A. Muller, and J. Bruley. Electron optical improvements are being carried out in collaboration with O. L. Krivanek, N. Dellby, H. W. Mook, and P. Kruit.

References

1. F. Stern and S. E. Laux, *Appl. Phys. Lett.* **61,** 1110 (1992).
2. K. Ismail, F. K. LeGoues, K. L. Saenger, M. Arafa, J. O. Chu, P. M. Mooney, and B. S. Meyerson, *Phys. Rev. Lett.* **73,** 3447 (1994).
3. B. Tomiyasu, I. Fukuju, H. Komatsubara, M. Owari, and Y. Nihei, *Nucl. Instrum. Meth. Phys. Res. B* **136–138,** 1028 (1998).
4. Y. Martin and H. K. Wickramasinghe, *Appl. Phys. Lett.* **64,** 2498 (1994).
5. J. P. Benedict, R. M. Anderson, and S. J. Klepeis, in *Advances and Applications in the Metallography and Characterization of Materials and Microelectronic Components*, International Metallographic Society (ASM, Int.), Materials Park, Ohio, 1996, pp. 277–284.
6. A. V. Crewe and J. Wall, *Optik* **30,** 407 (1970).
7. S. J. Pennycook and L. A. Boatner, *Nature* **336,** 565 (1988).
8. J. Silcox, P. Xu, and R. F. Loane, *Ultramicrosc.* **47,** 173 (1992).
9. Y. Ohtsuki, *Charged Beam Interaction with Solids*, Taylor and Francis, Ltd., London, 1983, p. 31.

10. R. F. Egerton, *Electron Energy Loss Spectroscopy in the Electron Microscope*, Plenum Press, New York, 1986.
11. P. E. Batson, K. L. Kavanagh, J. M. Woodall, and J. W. Mayer, *Phys. Rev. Lett.* **57,** 2729 (1986).
12. N. Yamamoto, J. C. H. Spence, and D. Fathy, *Phil. Mag. B* **49,** 609 (1984).
13. S. J. Pennycook, *Ultramicrosc.* **7,** 99 (1981).
14. U. Bangert, A. J. Harvey, D. Freundt, and R. Keyse, *J. Microsc.* **188,** 237 (1997).
15. P. E. Batson, *Ultramicrosc.* **78,** 33 (1999).
16. P. E. Batson, *Nature* **366,** 727 (1993).
17. D. A. Muller, T. Sorsch, S. Moccio, F. H. Baumann, K. Evans-Lutterodt, and G. Timp, *Nature* **399,** 758 (1999).
18. J. R. Chelikowsky and M. L. Cohen, *Phys. Rev. B* **14,** 556 (1976).
19. P. E. Batson, *J. Electron Microsc.* **45,** 51 (1996).
20. P. E. Batson and J. F. Morar, *Phys. Rev. Lett.* **71,** 609 (1993).
21. P. E. Batson and J. F. Morar, *Appl. Phys. Lett.* **59,** 3285 (1991).
22. J. F. Morar, P. E. Batson, and J. Tersoff, *Phys. Rev. B* **47,** 4107 (1993).
23. P. E. Batson, *Ultramicrosc.* **59,** 63 (1995).
24. P. E. Batson, in *Electron Microscopy and Analysis, Inst. of Phys. Conf. Ser. 147*, Institute of Physics, Bristol, England, 1995, pp. 169–174.
25. M. Paresi and S. Baroni, *Phys. Rev. B* **49,** 7490 (1994).
26. P. E. Batson and J. R. Heath, *Phys. Rev. Lett.* **71,** 911 (1993).
27. P. E. Batson, *Ultramicrosc.* **50,** 1 (1993).
28. O. L. Krivanek, N. Dellby, A. J. Spence, R. A. Camps, and L. M. Brown, in *Electron Microscopy and Analysis, Inst. of Phys. Conf. Ser. 153*, Institute of Physics, Bristol, England, 1997, pp. 35–40.
29. H. W. Mook, P. E. Batson, and P. Kruit, *Proceedings of EMAG '99*, Institute of Physics Conference Series No. 161, Institute of Physics, Bristol, England, 1999, pp. 223–226.
30. P. E. Batson, *J. Microsc.* **180,** 204 (1995).

Received June 3, 1999; accepted for publication December 20, 1999

Philip E. Batson *IBM Research Division, Thomas J. Watson Research Center, P.O. Box 218, Yorktown Heights, New York 10598 (batson@us.ibm.com).* Dr. Batson is a Research Staff Member in the Physical Sciences Department at the Thomas J. Watson Research Center. He received a B.S. degree in engineering physics and a Ph.D. degree in applied physics from Cornell University in 1970 and 1976, respectively. From 1976 until 1978 he worked in the area of imaging of magnetic structures at the Cavendish Laboratory in Cambridge, England, via a postdoctoral fellowship from Glasgow University. In 1978 he joined IBM at the Thomas J. Watson Research Center, where he has worked in the area of spatially resolved electron energy loss spectroscopy. In 1995 he received an IBM Outstanding Technical Achievement Award for achieving atomic resolution spectroscopy. He is an author or co-author of more than 140 technical papers. Dr. Batson is a member of the Microscopy Society of America and the American Association for the Advancement of Science. He is a Fellow of the American Physical Society and a member of the board of the New York State section of the American Physical Society.